Materials International
Open-Access Journal (ISSN: 2668-5728)

Article
Volume 7, Issue 3 2025, 22
https://doi.org/10.33263/Materials73.022

Structural and Dielectric analysis of (1-x) $Ni_{0.5}Cu_{0.25}Zn_{0.25}Fe_2O_4$ + (x) $SrFe_{11}Y_1O_{19}$ Soft-Hard Ferrite Nano-Composites

Vidyasagar Phase [1], Vishnu Shinde [2], Sanskruti Kadam [3], Kirti Desai [4], Anil Shitre [5], Ram Kadam [6,*]

1 Materials Science Research Laboratory, Shrikrishna College, Gunjoti, Dharashiv (M.S.) India; vidphase@gmail.com;
2 Chemistry Department, S. C. S. College, Omerga, Dharshiv (M.S.) India; drvisnhushinde@gmail.com;
3 Physics Department, Jawahar College, Anadur, Dharashiv (M.S.) India; sanskrutiskadam@gmail.com;
4 Physics Department, Balbhim College, Beed (M.S.) India; kirtidesai2702@gmail.com;
5 Physics Department, Y. C. College, Tuljapur, Dharashiv (M.S.) India; shitreanil09@gmail.com;
6 Materials Science Research Laboratory, Shrikrishna College, Gunjoti, Dharashiv (M.S.) India; ram111612@yahoo.co.in;
* Correspondence: ram111612@yahoo.co.in;

Received: 5.11.2024; Accepted: 27.07.2025; Published: 10.09.2025

Abstract: In this study, soft–hard ferrite nanocomposites of the composition (1–x) $Ni_{0.5}Cu_{0.25}Zn_{0.25}Fe_2O_4$ (NCZFO) + (x) $SrFe_{11}Y_1O_{19}$ (SFYO), with x ranging from 0.0 to 1.0, were synthesized via the sol-gel auto-combustion method to investigate their structural and dielectric properties. X-ray diffraction analysis confirmed the presence of distinct spinel and hexagonal phases without the formation of secondary phases. The crystallite sizes, calculated using the Scherrer equation, ranged from 24.31 to 19.66 nm for the soft phase and 19.76 to 23.83 nm for the hard phase. Dielectric measurements conducted in the frequency range of 50 Hz to 5 MHz revealed a typical dielectric dispersion behavior, with the dielectric constant decreasing as frequency increased. This behavior was attributed to interfacial polarization, grain boundary effects, and Fe^{2+}/Fe^{3+} ion exchange. The results demonstrate that these composites possess tunable dielectric properties and are promising candidates for use in high-frequency applications, such as electromagnetic interference (EMI) shielding and microwave devices.

Keywords: soft-hard nanocomposites; sol-gel autocombustion; nanoparticles; X-ray diffraction.

1. Introduction

Recent advancements in oxide materials research have gained significant momentum due to their broad applicability in various technological devices [1-3]. To address the increasing demand for sustainable functional materials, researchers are increasingly focusing on alloys and composite systems, as single-phase materials frequently fail to meet the diverse requirements of modern technologies [4-6]. The combination of soft and hard phases in oxide materials has attracted significant attention as a promising strategy to enhance performance and achieve multifunctional properties. Soft-hard composite ferrites, which incorporate both soft and hard magnetic phases, are an intriguing class of materials with a wide range of applications, including electromagnetic devices and data storage systems. The exploration of these ferrites

began in the mid-20th century when researchers started investigating materials with tailored properties. During the early 1950s, advances in ceramic technology led to the discovery and development of soft ferrites, which were valued for their high electrical resistivity and low coercivity. These properties made them ideal for immediate use in electronics, particularly in transformer cores and high-frequency devices, due to their low energy-loss characteristics [7-9].

Beyond their magnetic properties, the dielectric characteristics of soft-hard ferrite composites are of considerable importance, particularly for applications in microwave technology, communication systems, and energy storage. Ferrites are known for their high dielectric constants, low dielectric losses, and excellent insulating properties, making them ideal for capacitors, microwave components, and magnetic cores. The dielectric constant and loss in ferrite composites are influenced by several factors, including composition, grain size, sintering temperature, and operating frequency [10-13]. Additionally, by adjusting the proportion of soft and hard phases, the dielectric behavior of these materials can be optimized, enhancing the performance of devices such as antennas, filters, and oscillators [14].

NiCuZn ferrites are highly valued among soft magnetic materials, especially for high-frequency applications, due to their cost-effectiveness, high resistivity, and low eddy current losses. These properties have made them a focal point of research, particularly in the development of multilayer chip inductors. Their use in a wide range of electromagnetic devices stems from their excellent attributes, such as high resistivity, high permeability, and relatively low magnetic losses, which have garnered significant interest from the scientific community [15-18]. Researchers have experimented with various ratios of Ni, Cu, and Zn ions, and it has been reported that the composition $Ni_{0.5}Cu_{0.25}Zn_{0.25}Fe_2O_4$ demonstrates superior magnetic and electrical properties compared to other combinations in NiCuZn ferrites [19-21].

Conversely, $SrFe_{12}O_{19}$ hexaferrite is a widely recognized hard magnetic material. Hexaferrites with high magnetic anisotropy and low microwave losses play a crucial role in devices like circulators and isolators, which are vital for effective signal transmission and reception in communication technologies [22-24]. M-type hexaferrites, such as $SrFe_{12}O_{19}$ (commonly referred to as ceramic magnets), are distinguished by their magneto-plumbite structure, strong magnetocrystalline anisotropy, high saturation magnetization, and elevated Curie temperature. Although not as strong as rare earth magnets, strontium hexaferrites (SrM) exhibit a high Curie temperature of 733 K, exceeding the 583 K of commercial NdFeB magnets [25]. In addition, SrM magnets offer excellent chemical stability, resistance to external demagnetizing forces, immunity to humidity-induced corrosion, and are economically advantageous [26-28].

NiCuZn ferrite, a soft magnetic material with a spinel structure, is known for its high resistivity, low eddy current losses, and good thermal stability. These properties make it suitable for high-frequency applications, especially in miniaturized electronic components such as multilayer chip inductors. Conversely, $SrFe_{11}Y_1O_{19}$ is an M-type hexaferrite that exhibits hard magnetic behavior characterized by high coercivity, strong magnetocrystalline anisotropy, and excellent chemical and thermal stability. The substitution of Y^{3+} ions for Fe^{3+} enhances its structural and dielectric characteristics. Combining these soft and hard phases allows for tailored magnetic and dielectric responses, enabling the development of multifunctional composites suitable for electromagnetic interference (EMI) shielding, microwave absorbers, and high-frequency devices.

Various techniques have been employed to synthesize composites of hard and soft ferrites. Mehdipour *et al*. [29] synthesized $SrFe_{12}O_{19}NiFe_2O_4$ particles using a sodium hydroxide solution, demonstrating that differences in ferrite types and particle morphology led to a reduction in saturation magnetization and coercivity. Xu *et al* [30] utilized a wet chemical method to produce $SrFe_{12}O_{19}$/Fe–Co particles, providing insights into the formation mechanisms of core/shell structures. Among these methods, the sol-gel auto-combustion method was employed to synthesize soft-hard ferrite nanocomposites due to its distinct advantages over conventional techniques. This method allows precise control over stoichiometry, homogeneity, and particle size at the nanoscale, which is critical for achieving uniform distribution of both soft (NCZFO) and hard (SFYO) phases. The sol-gel process facilitates the formation of highly reactive precursors, enabling low-temperature synthesis and minimizing energy consumption. Additionally, the auto-combustion step ensures the formation of fine-grained, crystalline powders with minimal agglomeration, which is essential for optimizing dielectric and magnetic properties. The ability to tailor the microstructure and composition at the molecular level makes this method particularly suited for developing advanced nanocomposites with enhanced functional properties [31, 32].

The objective of this study is to synthesize soft-hard nanocomposites of (1-x) $Ni_{0.5}Cu_{0.25}Zn_{0.25}Fe_2O_4$ (NCZFO) + (x) $SrFe_{11}Y_1O_{19}$ (SFYO) using the sol-gel auto-combustion method. The main focus is to investigate the structural and dielectric properties of these nanocomposites as their weight ratio is varied.

2. Materials and Methods

2.1. Materials.

High-purity analytical grade (≈99.5%) metal nitrates of the required elements were used as starting materials. For synthesizing the soft ferrite phase (1-x) ($Ni_{0.5}Cu_{0.25}Zn_{0.25}Fe_2O_4$) nanoparticles, nickel nitrate ($Ni(NO_3)_2{\cdot}6H_2O$), copper nitrate ($Cu(NO_3)_2{\cdot}6H_2O$), zinc nitrate ($Zn(NO_3)_2{\cdot}6H_2O$), and iron nitrate ($Fe(NO_3)_3{\cdot}9H_2O$) were employed. Similarly, for the hard ferrite phase ($SrFe_{11}Y_1O_{19}$) nanoparticles, strontium nitrate ($Sr(NO_3)_2{\cdot}6H_2O$), ferric nitrate ($Fe(NO_3)_3{\cdot}9H_2O$), and yttrium nitrate ($Y(NO_3)_3{\cdot}9H_2O$) were used. Citric acid ($C_6H_8O_7$) acted as a chelating agent in both phases, while liquid ammonia was added to adjust the pH of the solutions.

2.2. Synthesis of the soft phase.

$Ni_{0.5}Cu_{0.25}Zn_{0.25}Fe_2O_4$ nanoparticles were prepared using the sol-gel auto-combustion technique. High-purity metal nitrates (99%)—nickel nitrate ($Ni(NO_3)_2{\cdot}6H_2O$), copper nitrate ($Cu(NO_3)_2{\cdot}3H_2O$), zinc nitrate ($Zn(NO_3)_2{\cdot}6H_2O$), and iron nitrate ($Fe(NO_3)_3{\cdot}9H_2O$)—along with citric acid ($C_6H_8O_7$) were utilized as raw materials. The nitrates and citric acid were measured according to stoichiometric ratios, dissolved in distilled water, and mixed in a 1:3 molar ratio. The solution was stirred at 500 rpm while heating, and ammonia was added gradually to bring the pH to 7. The temperature was kept constant at 90°C. After 3 hours of stirring, a thick brown gel formed. Once the stirring stopped, the gel ignited on its own, producing ash after a short period. This ignition process lasted about 3 minutes. The resulting ash was finely ground and calcined at 800°C for 6 hours in a furnace, after which the powder was reground and stored for further use.

2.3. Synthesis of the hard phase.

Yttrium-substituted strontium hexaferrite ($SrFe_{11}Y_1O_{19}$) was produced through a sol-gel auto-combustion method. The starting materials included analytical-grade strontium nitrate ($Sr(NO_3)_2$), ferric nitrate ($Fe(NO_3)_3 \cdot 9H_2O$), and yttrium nitrate ($Y(NO_3)_3 \cdot 9H_2O$), all mixed in their stoichiometric amounts. These nitrates were dissolved in distilled water to ensure uniformity, and the mixture was stirred on a magnetic stirrer at 90°C. Citric acid was introduced in a 1:3 molar ratio relative to the nitrates while the solution was continuously stirred. Ammonia was carefully added to adjust the pH to around 7. After 2 to 3 hours, a gel began to form. Combustion occurred when the gel, heated to 150°C, produced a fine powder of yttrium-substituted strontium hexaferrite. This powder was sintered in a muffle furnace at 900°C for 6 hours, then cooled to room temperature. The sintered material was ground for 30 minutes to ensure homogeneity.

2.4. Synthesis of soft–hard nanocomposite.

The nanocomposite, consisting of (1-x) $Ni_{0.5}Cu_{0.25}Zn_{0.25}Fe_2O_4$+ (x) $SrFe_{11}Y_1O_{19}$, where x values were set to 0.0, 0.2, 0.4, 0.6, 0.8, and 1.0, was synthesized to achieve both soft and hard magnetic properties. The process began with the physical mixing of the NCZFO and SFYO phases, which had been synthesized earlier via the sol-gel auto-combustion method. The powders of both phases were mixed together and ground manually using an agate mortar and pestle for 30 minutes. After thorough grinding, the mixtures were calcined at 1000°C to complete the synthesis. The resulting powders were then prepared for further analysis and characterization.

2.5. Characterizations.

The phases and crystal structures of the samples were analyzed using an X-ray diffractometer, specifically the Goniometer Ultima IV, with Cu-Kα radiation having a wavelength of 1.5404 Å. Scanning was performed over a range from 20° to 80°. The dielectric properties of the samples were examined by first fabricating silver-coated discs and then analyzing them using a Hioki HiTESTER 3532-50.

3. Results and Discussion

3.1. Structural analysis.

Figure 1 illustrates the X-ray diffraction (XRD) patterns for the materials studied. Plots A and F show the XRD patterns for pure $Ni_{0.5}Cu_{0.25}Zn_{0.25}Fe_2O_4$ (NCZFO) and $SrFe_{11}Y_1O_{19}$ (SFYO), respectively. The XRD patterns B–E represent the composites of NCZFO and SFYO at various weight ratios. Plot A displays diffraction peaks corresponding to the cubic spinel structure of NCZFO, with key peaks indexed to planes (220), (311), (222), (400), (422), (511), and (440), consistent with the standard database (COD No. 9006895). Plot F shows diffraction peaks indexed to planes (110), (107), (114), (201), (203), (205), (206), (300), (217), (2011), and (1015), corresponding to the hexagonal crystal structure of SFYO, as per the standard database (COD No. 1561394). The patterns B–E reveal that the soft-hard ferrite nanocomposites retain both the hexaferrite and spinel phases without showing any new phases or structural changes, indicating that the synthesis method effectively preserves the distinct structures of both phases.

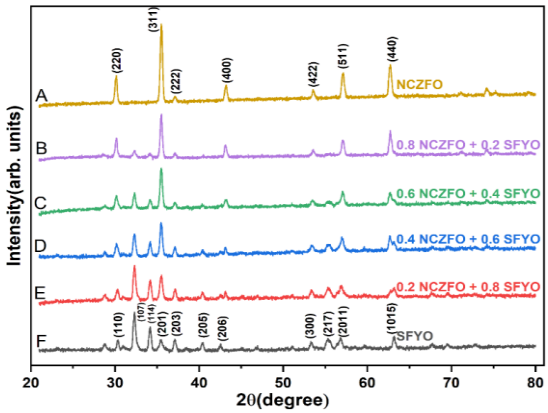

Figure 1. X-ray diffraction patterns of pure $Ni_{0.5}Cu_{0.25}Zn_{0.25}Fe_2O_4$ (soft phase), pure $SrFe_{11}Y_1O_{19}$ (hard phase), and (1-x) NCZFO + (x) SFYO composites.

Table 1 presents the structural parameters derived from Powder-X software. For the NCZFO phase, the lattice parameter ranges from 8.3814 Å to 8.3903 Å. In the case of the SFYO phase, the lattice parameters are observed with 'a' ranging from 5.9067 Å to 5.9227 Å and 'c' ranging from 23.0815 Å to 23.3395 Å. The data indicate that there is no direct correlation between the lattice constant variations and the weight percentage of the soft-hard ferrite composites.

Table 1. Lattice parameters (a, c) and crystallite size (t) for (1-x) NCZFO + (x) SFYO composites.

'x'	Lattice parameter		
	NCZFO	SFYO	
	'a' (Å) (±0.002)	'a' (Å) (±0.002)	'c' (Å) (±0.003)
0.0	8.3903	---	---
0.2	8.3884	5.9227	23.0815
0.4	8.3859	5.9188	23.1319
0.6	8.3835	5.9159	23.2051
0.8	8.3814	5.9127	23.2567
1.0	---	5.9067	23.3395

The crystallite sizes in both phases are determined using the relation discussed elsewhere [33]. The crystallite size for both phases is observed within the nanometer range. The average crystallite size obtained from the Scherrer relation decreased (from 24.31 to 19.66 nm) for the soft NCZFO phase, whereas it increased (from 19.76 to 23.83 nm) for the hard SFYO phase. Fig. 2 represents the variation of crystallite size of soft and hard phases.

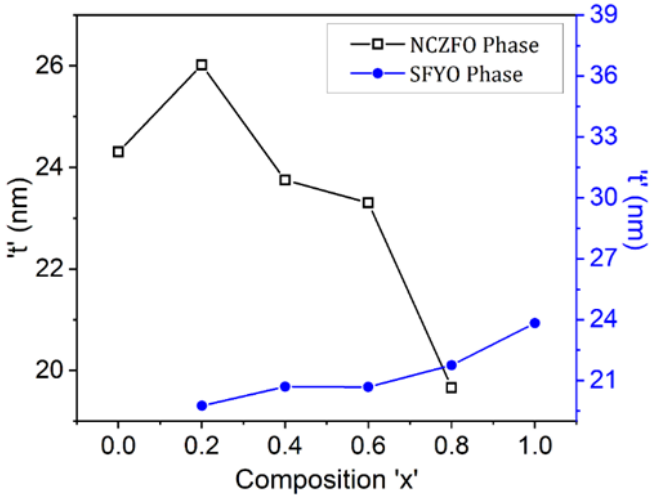

Figure 2. Variation of crystallite size of soft and hard phases.

3.2. Dielectric measurements.

Dielectric measurements were performed over a frequency range of 50 Hz to 5 MHz using a Hioki HiTESTER 3532-50 impedance analyzer at room temperature. The samples were formed into circular disc-shaped pellets, with a silver coating applied to the opposite faces to create a parallel-plate capacitor configuration, in which the ferrite material served as the dielectric medium. Figs. 3 and 4 illustrate the variation of the dielectric constant and dielectric loss tangent for all (1-x) $Ni_{0.5}Cu_{0.25}Zn_{0.25}Fe_2O_4$ (NCZFO) + (x) $SrFe_{11}Y_1O_{19}$ composites, including individual ferrite samples. All compositions exhibit dielectric dispersion, in which the dielectric constant decreases with increasing frequency at low frequencies and becomes nearly frequency-independent at higher frequencies.

The dielectric response shows strong dependence on microstructural characteristics arising from the composite nature of the system. The observed composition-dependent trends in ε' can be attributed to three key factors: (1) nanoscale grain dimensions (19-24 nm) that enhance surface-to-volume ratios and associated polarization effects, (2) varying interface density between spinel and hexagonal phases that creates additional polarization sites, and (3) differences in charge carrier mobility between the soft (high conductivity) and hard (low conductivity) phases. The progressive replacement of conductive NCZFO with insulating SFYO (increasing x) systematically modifies these factors, leading to the measured dielectric behavior. This interpretation aligns with Maxwell-Wagner interfacial polarization theory for heterogeneous systems [34,35].

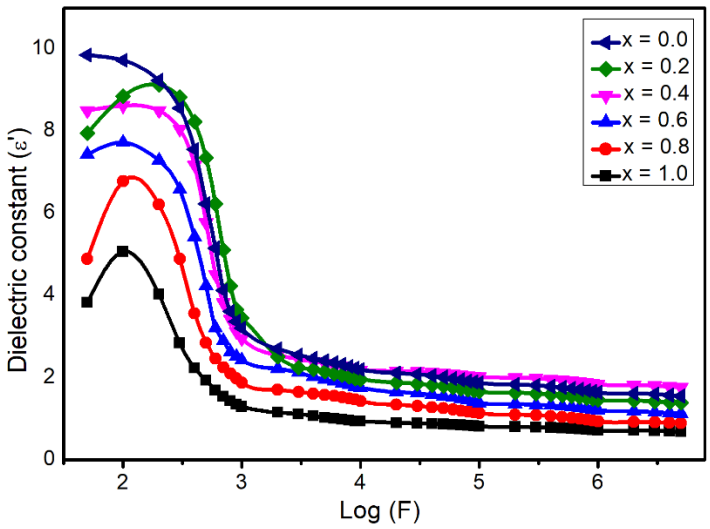

Figure 3. Variation of dielectric constant with frequency.

In our measurements, the dielectric constant (ε') is large in pure soft ferrite, but decreases with the addition of hard ferrite. The reduction in dielectric constant with increasing frequency is a typical behavior in ferromagnetic materials. In ferrites, polarization arises from electron hopping between Fe^{2+} and Fe^{3+} ions, leading to a localized shift of electrons along the direction of the applied electric field, thereby initiating the polarization mechanism. As the frequency increases, space charge carriers take longer to align with the alternating field, leading to a decrease in the dielectric constant. At even higher frequencies, space charge polarization contributes very little, resulting in a minimal effect on the dielectric constant [36]. The high dielectric constant at lower frequencies is mainly due to factors such as Fe^{2+} ions, oxygen vacancies, and grain boundary defects. However, as frequency increases, the polarizable

species begin to lag behind the applied field, naturally leading to a decrease in the dielectric constant [37].

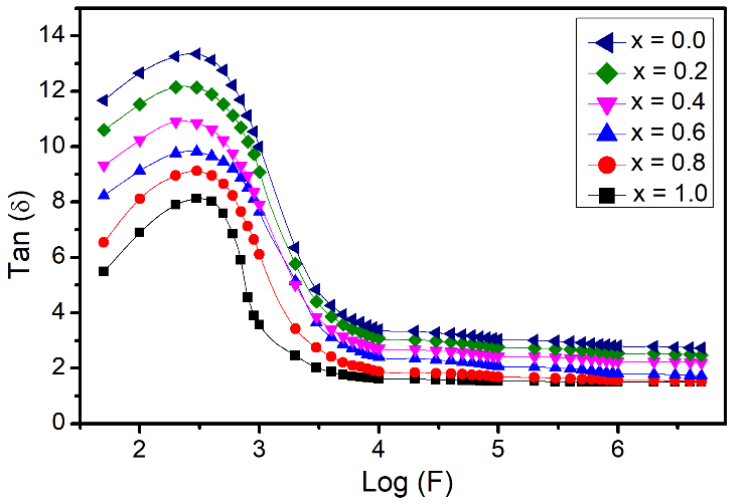

Figure 4. Variation of dielectric loss tangent with frequency.

Figure 4 shows the frequency-dependent behavior of the dielectric loss tangent measured at room temperature. The dielectric loss tangent represents the energy dissipated from the applied field into the sample, primarily due to domain wall resonance. Therefore, as the concentration of the hard phase increases, the dielectric loss tangent should also decrease. This is because there will be less contribution from the conductive pathways and dipolar relaxation processes prevalent in the soft phase. At higher frequencies, losses are reduced because domain wall motion is restricted, forcing magnetization to change via rotation. A strong correlation exists between the conduction process and the dielectric properties of ferrites. [38].

4. Conclusions

In this study, we successfully synthesized (1-x)$Ni_{0.5}Cu_{0.25}Zn_{0.25}Fe_2O_4$ + (x)$SrFe_{11}Y_1O_{19}$ nanocomposites via the sol-gel auto-combustion method, achieving a homogeneous distribution of soft (spinel) and hard (hexagonal) phases without secondary phase formation. XRD analysis revealed that the lattice parameters of both phases varied systematically with composition, while crystallite sizes for the soft phase decreased (24.31 → 19.66 nm) and increased for the hard phase (19.76 → 23.83 nm), reflecting phase-specific structural adjustments.

The dielectric properties of these composites exhibited frequency-dependent dispersion, with high dielectric constants (ε') at low frequencies (50 Hz–1 kHz) attributed to interfacial polarization, Fe^{2+}/Fe^{3+} hopping, and grain boundary effects. Notably, the ε' values decreased with increasing hard-phase content, suggesting tunability for specific applications. The low dielectric loss (tan δ) at higher frequencies (1–5 MHz) further underscores their suitability for high-frequency devices, such as antennas, filters, and electromagnetic shielding materials.

Variations in the dielectric constant and loss tangent with composition indicated that the ratio of soft to hard ferrites influences the dielectric performance. This variability highlights the ability to tailor the dielectric properties of these composites by adjusting their compositional ratio to suit specific applications. These findings set the stage for further exploration of these materials for electronic and magnetic applications, with potential to optimize performance

based on desired dielectric and structural characteristics. Future research will aim to employ additional characterization techniques and assess the practical applications of these ferrite composites, including their use in high-frequency devices, electromagnetic interference shielding, and energy storage systems.

Author Contributions

Conceptualization, R.K.; methodology, V.P.; software, V.S.; validation, R.K. and V.P.; formal analysis, V.P. and S.K.; investigation, S.K.; resources, V.S. and K.D.; data curation, R.K. and K.D.; writing—original draft preparation, V.P. and A.S.; writing—review and editing, R.K.; supervision, A.S. All authors have read and agreed to the published version of the manuscript.

Institutional Review Board Statement

Not applicable.

Informed Consent Statement

Not applicable.

Data Availability Statement

Data supporting the findings of this study are available upon reasonable request from the corresponding author.

Funding

This research received no external funding.

Acknowledgments

Author Vidysagar Phase is thankful to the Research Center in Physics, Shrikrishna College, Gunjoti, for providing experimental facilities.

Conflicts of Interest

The authors declare no conflict of interest.

References

1. Zhang, X.; Tang, Y.; Zhang, F.; Lee, C.S. A Novel Aluminium-Graphite dual-ion battery. *Adv. Energy Mater.* **2016**, *6*, 1502588, https://doi.org/10.1002/aenm.201502588.
2. Zhang, J.; Wang, X.; Zhou, L.; Liu, G.; Adroja, D.T.; da Silva, I.; Demmel, F.; Khalyavin, D.; Sannigrahi, J.; Nair, H.S. A ferrotoroidic candidate with well-separated spin chains. *Adv. Mater.* **2022**, *34*, 2106728, https://doi.org/10.1002/adma.202106728.
3. Wang, K.; Zhu, J.; Wang, H.; Yang, K.; Zhu, Y.; Qing, Y.; Ma, Z.; Gao, L.; Liu, Y.; Wei, S. Air plasma-sprayed high-entropy $(Y_{0.2}Yb_{0.2}Lu_{0.}2Eu_{0.2}Er_{0.2})_3Al_5O_{12}$ coating with high thermal protection performance. *J. Adv. Ceram.* **2022**, *11*, 1571-1582, https://doi.org/10.1007/s40145-022-0630-2.
4. Yang, B.; Wang, H., Zhang, M.; Jia, F.; Liu, Y.; Lu, Z. Mechanically strong, flexible, and flame – retardant $Ti_3C_2T_x$ MXene – coated aramid paper with superior electromagnetic interference shielding and electrical heating performance. *Chem. Eng. J.* **2023**, *476*, 146834, https://doi.org/10.1016/j.cej.2023.146834.

5. Long, X.; Chong, K.; Su, Y.; Chang, C.; Zhao, L. Meso-scale low-cycle fatigue damage of polycrystalline nickel-based alloy by crystal plasticity finite element method. *Int. J. Fatigue* **2023**, *175*, 107778, https://doi.org/10.1016/j.ijfatigue.2023.107778.
6. Phase, V.P.; Kammar, S.S.; Munnoli, C.S.; Madansure, Y.S.; Ibrahim, A.A.; Batoo, K.M.; Kadam, R.H.; Shirsath, S.E.; Shitre, A.R. Strain and exchange – spring mechanism of (1-*x*) $Ni_{0.5}Cu_{0.25}Zn_{0.25}Fe_2O_4$ + (*x*) $SrFe_{11}Y_1O_{19}$ magnetically soft-hard ferrite composed nanoparticles. *Part. Part. Syst. Char.* **2024**, *41*, 2300225, https://doi.org/10.1002/ppsc.202300225.
7. Esir, S.; Junejo, Y.; Baykal, A.; Toprak, M.; Sözeri, H. $SrFe_{12}O_{19}/Zn_{0.65}Ni_{0.25}Cu_{0.1}Fe_2O_4$ Core–Shell Nanocomposite: Synthesis, Chracterization and Catalytic Activity in Aqueous Solution. *J. Inorg. Organomet. Polym. Mater.* **2014**, *24*, 722-728, https://doi.org/10.1007/s10904-014-0031-2.
8. Gaikwad, A.S.; Kadam, R.H.; Shirsath, S.E.; Wadgane, S.R.; Shah, J.; Kotnala, R.K. Kadam, A.B. Surprisingly high magneto-electric coupling in cubic $Co_{0.7}Fe_{2.3}O_4$ – $SrTiO_3$ nano-composites. *J. Alloys Compd.* **2019**, *773*, 564-570, https://doi.org/10.1016/j.jallcom.2018.09.209.
9. Shitole, R. S.; Barote, V. K.; Mane, M. L.; Alone, S. T.; Batoo, K. M.; Hussain, S.; Kadam, R. H. Elastic and dielectric properties of nano-crystalline Dy^{3+} substituted zinc–chromium ferrite. *J. Mater. Sci. Mater. Electron.* **2023**, *34*, 1106, https://doi.org/10.1007/s10854-023-10531-6.
10. Almessiere, M.A.; Slimani, Y.; Ibrahim, Y.O.; Gondal, M.A.; Dastageer, M.A.; Auwal, I.A.; Trukhanov, A.V.; Manikandan, A.; Baykal, A. Morphological, structural, and magnetic characterization of hard-soft ferrite nanocomposites synthesized via pulsed laser ablation in liquid. *Mater. Sci. Eng. B* **2021**, *273*, 115446, https://doi.org/10.1016/j.mseb.2021.115446.
11. Gurav, S.K.; Shirsath, S.E.; Kadam, R.H.; Mane, D.R. Low temperature synthesis of $Li_{0.5}Zr_xCo_xFe_{2.5-2x}O_4$ powder and their characterization. *Powder Technol.* **2013**, *235*, 485-492, https://doi.org/10.1016/j.powtec.2012.11.009.
12. Jotania, R.B.; Nandotaria, R.A.; Chauhan, C.C.; Hashim, M.; Meena, S.S.; Shirsath, S.E. Magnetic and structural properties of spinel ferrites. *Ceram. Int.* **2016**, *42*, 2289-2298, https://doi.org/10.1016/j.ceramint.2015.10.023.
13. Almessiere, M.A.; Unal, B.; Demir Korkmaz, A.; Shirsath, S. E.; Baykal, A.; Slimani, Y.; Gondal, M. A.; Baig, U.; Trukhanov, A. V. Electrical and dielectric properties of rare earth substituted hard-soft ferrite $(Co_{0.5}Ni_{0.5}Ga_{0.01}Gd_{0.01}Fe_{1.98}O_4)_x/(ZnFe_2O_4)_y$ nanocomposites. *J. Mater. Res. Technol.* **2021**, *15*, 969-983, https://doi.org/10.1016/j.jmrt.2021.08.049.
14. Zhu, S.; Huang, K.; Ni, J.; Kan, X.; Lv, Q.; Cheng, Y.; Feng, S.; Liu, X. Magnetic and microwave absorption properties of $Ni_{0.6}Zn_{0.4}Fe_2O_4$ /$SrFe_{12}O_{19}$ composites. *Mater. Chem. Phys.* **2022**, *288*, 126398, https://doi.org/10.1016/j.matchemphys.2022.126398.
15. Balsure, S.; More, V.; Kadam, S.; Kadam, R.; Kadam, A. Synthesis, Structural, Magnetic, Dielectric and Optical Properties of Co Doped Cr-Zn Oxide Nanoparticles for Spintronic Devices. *Eng. Sci.* **2022**, *21*, 774, http://dx.doi.org/10.30919/es8d774.
16. Singhal, S.; Chandra, K. Magnetic and Mössbauer spectral studies of *x* ($NiFe_2O_4$) + (1−*x*)($SrFe_{12}O_{19}$), *x* = 0, 0.2, 0.4, 0.6, 0.8 and 1.0 nanocomposites. *Hyperfine Interact.* **2008**, *183*, 93-97, https://doi.org/10.1007/s10751-008-9735-4.
17. Mehdipour, M.; Shokrollahi, H.; Bahadoran, A. Investigating the Exchange-Coupling Interaction in Nanostructure Composite Particles of $SrFe_{12}O_{19}$ and $ZnFe_2O_4$. *J. Electron. Mater.* **2014**, *43*, 4282-4288, https://doi.org/10.1007/s11664-014-3363-3.
18. Choudhari, S.S.; Shelke, S.B.; Batoo, K.M.; Adil, S.F.; Kadam, A.B.; Imran, A.; Hadi, M.; Raslan, E.H.; Shirsath, S.E.; Kadam, R.H. $Mn_{0.7}Zn_{0.3}Fe_2O_4 + BaTiO_3$ composites: structural, morphological, magnetic, M–E effect and dielectric properties. *J. Mater. Sci. Mater. Electron.* **2021**, *32*, 10308-10319, https://doi.org/10.1007/s10854-021-05686-z.
19. Almessiere, M.A.; Caliskan, S.; Baykal, A.; Klygach, D.S.; Trukhanov, S.V.; Slimani, Y.; Zubar, T.I.; Vinnik, D.A.; Trukhanov, A.V.; Arslan, E. Impact of Ho substitution on structure, magnetic and electromagnetic properties of hard-soft nanocomposites. *Mater. Sci. Eng. B* **2024**, *308*, 117571, https://doi.org/10.1016/j.mseb.2024.117571.
20. Hashim, M.; Shirsath, S.E.; Kumar, S.; Kumar, R.; Roy, A.S.; Shah, J.; Kotnala, R.K. Preparation and characterization chemistry of nano-crystalline Ni–Cu–Zn ferrite. *J. Alloys Compd.* **2013**, *549*, 348-357, https://doi.org/10.1016/j.jallcom.2012.08.039.

21. Hashim, M.; Shirsath, S. E.; Meena, S. S.; Kotnala, R. K.; Kumar, S.; Ravinder, D.; Raghasudha, M.; Bhatt, P.; Şentürk, E.; Kumar, R. Superparamagnetic behavior of indium substituted NiCuZn nano ferrites. *J. Magn. Magn. Mater.* **2015**, *381*, 416-421, https://doi.org/10.1016/j.jmmm.2015.01.021.
22. Slimani, Y.; Almessiere, M.A.; Shirsath, S. E.; Hannachi, E.; Yasin, G.; Baykal, A.; Ozcelik, B.; Ercan, I. Investigation of structural, morphological, optical, magnetic and dielectric properties of (1-*x*)$BaTiO_3$/*x*$Sr_{0.92}Ca_{0.04}Mg_{0.04}Fe_{12}O_{19}$ composites. *J. Magn. Magn. Mater.* **2020**, *510*, 166933, https://doi.org/10.1016/j.jmmm.2020.166933.
23. Satpute, S.S.; Wadgane, S.R.; Kadam, S.R.; Mane, D.R.; Kadam, R.H. Y^{3+} substituted Sr-hexaferrites: sol-gel synthesis, structural, magnetic and electrical characterization. *Cerâmica* **2019**, *65*, 274, https://doi.org/10.1590/0366-69132019653742582.
24. Praveena, K.; Sadhana, K.; Liu, H.-L.; Bououdina, M. Microwave absorption studies of magnetic sublattices in microwave sintered Cr^{3+} doped $SrFe_{12}O_{19}$. *J. Magn. Magn. Mater.* **2017**, *426*, 604-614, https://doi.org/10.1016/j.jmmm.2016.11.013.
25. Liu, C.; Kan, X.; Liu, X.; Feng, S.; Hu, J.; Wang, W.; Rehman, K. M.; Shezad, M. Influence of the Eu substitution on the structure and magnetic properties of the Sr-hexaferrites. *Ceram. Int.* **2020**, *46*, 171-179, https://doi.org/10.1016/j.ceramint.2019.08.245.
26. Almessiere, M.A.; Güner, S.; Slimani, Y.; Hassan, M.; Baykal, A.; Gondal, M. A.; Baig, U.; Trukhanov, S.V.; Trukhanov, A.V. Structural and Magnetic Properties of $Co_{0.5}Ni_{0.5}Ga_{0.01}Gd_{0.01}Fe_{1.98}O_4$/$ZnFe_2O_4$ Spinel Ferrite Nanocomposites: Comparative Study between Sol-Gel and Pulsed Laser Ablation in Liquid Approaches. *Nanomaterials* **2021**, *11*, 2461, https://doi.org/10.3390/nano11092461.
27. Kang, Y.-M.; Moon, K. Magnetic properties of Ce–Mn substituted M-type Sr-hexaferrites. *Ceram. Int.* **2015**, *41*, 12828-12834, https://doi.org/10.1016/j.ceramint.2015.06.119.
28. Xie, T.; Xu, L.; Liu, C.; Wang, Y. Magnetic composite $ZnFe_2O_4$/$SrFe_{12}O_{19}$: Preparation, characterization, and photocatalytic activity under visible light. *Appl. Surf. Sci.* **2013**, *273*, 684-691, https://doi.org/10.1016/j.apsusc.2013.02.113.
29. Mehdipour, M.; Shokrollahi, H. Comparison of microwave absorption properties of $SrFe_{12}O_{19}$, $SrFe_{12}O_{19}$/$NiFe_2O_4$, and $NiFe_2O_4$ particles. *J. Appl. Phys.* **2013**, *114*, 043906, https://doi.org/10.1063/1.4816089.
30. Xu, X.; Park, J.; Hong, Y.-K.; Lane, A.M. Magnetically self-assembled $SrFe_{12}O_{19}$/Fe–Co core/shell particles. *Mater. Chem. Phys.* **2015**, *152*, 9-12, https://doi.org/10.1016/j.matchemphys.2014.11.061.
31. Palmero, P. Structural ceramic nanocomposites: a review of properties and powders' synthesis methods. *Nanomaterials* **2015**, *5*, 656–696, https://doi.org/10.3390/nano5020656.
32. Parauha, Y.R.; Sahu, V.; Dhoble, S.J. Prospective of combustion method for preparation of nanomaterials: A challenge. *Mater. Sci. Eng. B* **2021**, *267*, 115054, https://doi.org/10.1016/j.mseb.2021.115054.
33. Shitole, R.S.; Barote, V.K.; Kadam, S.B.; Kadam, S.S.; Wadgane, S.R.; Shinde, V.S.; Hussain, S.; Batoo, K.M.; Shirsath, S.E.; Kadam, R.H. Williamson-Hall strain analysis, cation distribution and magnetic interactions in Dy^{3+} substituted zinc-chromium ferrite. *J. Magn. Magn. Mater.* **2023**, *588*, 171468, https://doi.org/10.1016/j.jmmm.2023.171468.
34. Koops, C.G. On the dispersion of resistivity and dielectric constant of some semiconductors at audio frequencies. *Phys. Rev.* **1951**, *83*, 121, https://doi.org/10.1103/PhysRev.83.121.
35. Prodromakis, T.; Papavassiliou, C.J. Engineering the Maxwell–Wagner polarization effect. *Appl. Surf. Sci.* **2009**, *255*, 6989–6994, https://doi.org/10.1016/j.apsusc.2009.03.030.
36. Murthy, V.R.K.; Sobhanadri, J. Dielectric properties of some nickel-zinc ferrites at radio frequency. *Phys. Status Solidi A* **1976**, *36*, K133-K135, https://doi.org/10.1002/pssa.2210360247.
37. Maxwell, J.C. A Treatise on Electricity and Magnetism; Clarendon Press: **1873**.
38. Iwauchi, K.; Ikeda, Y. Dielectric Properties of Hexagonal Ferrites. *Phys. Status Solidi A* **1986**, *93*, 309–313, https://doi.org/10.1002/pssa.2210930138.

Publisher's Note & Disclaimer